# Structural data constraints for implicit modeling of folds

Lachlan Grose, Gautier Laurent, Laurent Ailleres, Robin Armit, Mark W. Jessell, Guillaume Caumon

*Journal of Structural Geology*, 104: 80–92, 2017
10.1016/j.jsg.2017.09.013

# Structural Data Constraints for Implicit Modeling of Folds

Lachlan Grose*[1], Gautier Laurent[1,2], Laurent Ailleres[1], Robin Armit[1], Mark Jessell[3], and Guillaume Caumon[2]

[1]*School of Earth, Atmosphere and Environment, Monash University PO Box 28E, Victoria, Australia*
[2]*GeoRessources (UMR 7359), Université de Lorraine-ENSG, CNRS,CREGU, Campus Brabois, Vandoeuvre-lès-Nancy Cedex, France*
[3]*The University of Western Australia, Centre for Exploration Targeting, , School of Earth and Environment, Perth, Western Australia, Australia*

**Abstract** A recent method for modeling folds uses a fold frame with coordinates based on the structural geology of folds: fold axis direction, fold axial surface and extension direction. The fold geometry can be characterised by rotating the fold frame by the pitch of the fold axis in the axial surface and the angle between the folded foliation and the axial surface. These rotation angles can be expressed as 1D functions of the fold frame coordinates. In this contribution we present methods for extracting and automatically modeling the fold geometries from structural data. The fold rotation angles used for characterising the fold geometry can be calculated locally from structural observations. The fold rotation angles incorporate the structural geology of the fold and allow for individual structural measurements to be viewed in the context of the folded structure. To filter out the effects of later folding the fold rotation angles are plotted against the coordinates of the fold frame. Using these plots the geometry of the folds can be interpolated directly from structural data where we use a combination of radial basis function and harmonic analysis to interpolate and extrapolate the fold geometry. This contribution addresses a major limitation in existing methods where the fold geometry was not constrained from structural data. We present two case studies: a proof of concept synthetic model of a non-cylindrical fold and an outcrop of an asymmetrical fold within the Lachlan Fold belt at Cape Conran, Victoria, Australia.

**Keywords**
Folds
Foliation
Vergence
Geometrical Modeling

## 1 Introduction

Folds are one of the most common features found in deformed rocks [Ramsay and Huber, 1987] but still present a challenge for three-dimensional structural modeling because the geometry of folded surfaces cannot be characterised from individual structural observations. Folds produce localised variations in curvature [Lisle and Toimil, 2007; Mynatt et al., 2007], however interpolation algorithms at the base of structural modeling generally fit a surface of minimal curvature [Jessell et al., 2014; Laurent et al., 2016]. To model folded surfaces, the geologist is often required to use additional cross sections, level maps or other interpretive constraints such as synthetic bore holes to produce the expected geometry [Caumon et al., 2003; Jessell et al., 2010, 2014]. This approach has proven operative in practice, but it is often cumbersome and reduces the objectivity and reproducibility of the modeling process. Most interpolation algorithms only consider local orientation of the surface and cannot incorporate any additional structural information or geological knowledge. These methods do not incorporate all available structural information collected by field geologists such as: lineations, foliations, overprinting relationships, fold axis, fold axial surface and vergence. This additional structural information can provide excellent constraints on complicated geometries found in hard rock terranes [Laurent et al., 2016].

In implicit modeling systems, geological surfaces such as lithological contacts, fold axial surfaces or fault surfaces are represented by isovalues of a global scalar field [Cowan et al., 2003; Frank et al., 2007; Calcagno et al., 2008; Hillier et al., 2014]. The scalar field is interpolated using some of the available geological observations (*e.g.* orientation, lithology type, structural trend). A number of different interpolation methods exist [Cowan et al., 2003; Moyen et al., 2004; Aug et al., 2005; Frank et al., 2007; Calcagno et al., 2008; Caumon et al., 2013]. These methods typically consider the final state of deformation and attempt to produce final 3D fold geometry from spatial measurements such as form lines, and strike and dip measurements. However, these methods generally use variants of isotropic Laplacian minimization, which is only appropriate when spatial observations are densely sampled. In sparse data settings, this isotropic assumption tends to generate structural geometries that are incompatible with the strong curvature anisotropy classically observed in folded terrains [Lisle and Toimil, 2007; Mynatt et al., 2007] and are highly non-developable [Thibert et al., 2005].

The problem of geometrically modeling folds has been addressed by a number of authors [Hillier et al., 2014; Laurent et al., 2016; Massiot and Caumon, 2010; Maxelon et al., 2009; Thibert et al., 2005]. These approaches have provided the framework to incorporate the fold axial surface [Laurent et al., 2016; Maxelon et al., 2009; Thibert et al., 2005], fold axis [Massiot and Caumon, 2010; Hillier et al., 2014; Laurent et al., 2016] and a description of fold geometry and overprinting relationships [Laurent et al., 2016]. Laurent et al. [2016] introduced a global fold frame which provides a reference coordinate system for each deformational event based on the structural elements of the fold. This allows for the geometry of older folds to be described without the effects of younger deformation events. For each folding event two rotation angles are calculated from field data: (1) the fold axis rotation angle, and (2) the fold limb rotation angle. To parametrise the variations of these two angles with respect to the fold frame, Laurent et al. [2016] use a periodical fold shape, which depends on estimations of fold wavelength, amplitude and location of fold hinge. In Laurent et al. [2016] these parameters are inferred using trial and error.

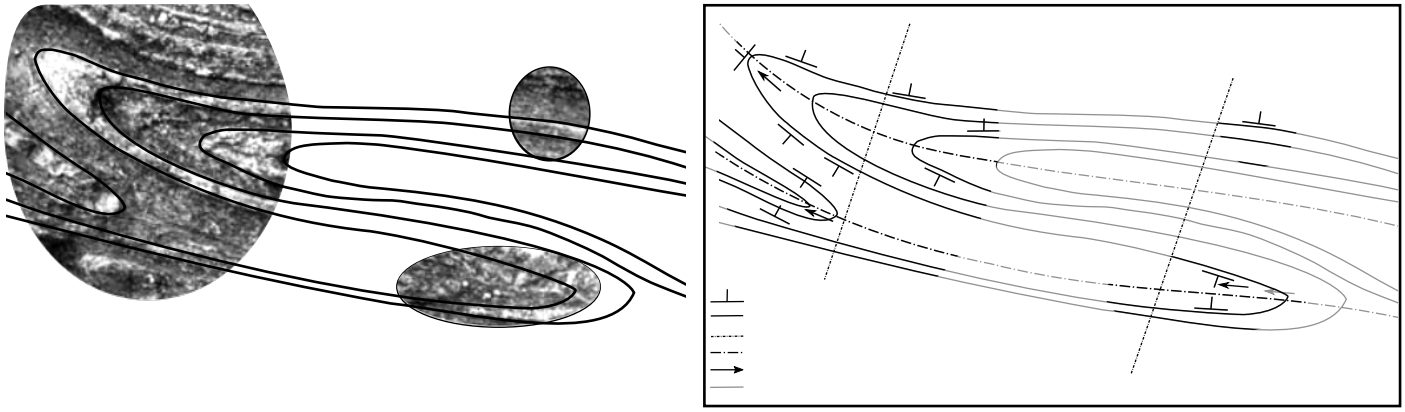

**Figure 1** A: Outcrop from Kinlochleven, Scotland of a refolded fold [Hilgers, 2006]. B: A schematic sketch showing the possible structural observations that could be collected from key locations highlighted areas in (A). The fold hinges are located at the intersection between $S_0$ and $S_1$ form lines, the fold axis is cannot be observed in the photograph and the $S_1$ form lines represent the intersection between the axial surface and the outcrop surface. Light lines represent a possible interpretation between these key locations.

In this contribution, we present a method for directly extracting and characterising the geometry of folds from field data. The two fold rotation angles that are necessary for characterising a fold geometry can be calculated locally from field observations and interpolated throughout the modeled volume using multiple scalar and vector fields. We present two approaches for characterising the fold rotation angles within the fold frame: (1) standard interpolation, where there is enough structural data to characterise the fold shape, or; (2) a combined interpolation and extrapolation method using a Fourier series to represent the fold geometry. Where insufficient observations exist to characterise the geometry of the fold throughout the model volume, the Fourier series approximation of the fold geometry provides a geologically reasonable estimate that is objectively defined by the structural observations. We demonstrate these approaches on: (1) a synthetic example of a doubly plunging fold series, and (2) asymmetrical folds from Cape Conran, Victoria.

## 2 Related work

### 2.1 Structural Geology of Folds

Structural geologists describe the geometry of folds using the geometrical characteristics of the folded surfaces [Ramsay and Huber, 1987, p. 311-317]: (1) the fold hinge is the location of maximum curvature for the folded surface, (2) the axial surface separates opposing limbs and contains fold hinges of conformable surfaces, and (3) the fold axis as either the fold hinge line or the line of intersection between the folded foliation and the axial foliation.

A planar fabric can often be observed orthogonal to the direction of principal shortening and roughly parallel to the fold axial surface [Ramsay and Huber, 1987; Hudleston and Treagus, 2010]. The foliation can be used in a general case, to characterise the geometry of the axial surface away from fold hinges. This fabric is often pervasive and is commonly recorded by geologists to map the geometry of the fold axial surface. The intersection of this foliation and any older folded foliation provides a lineation that is parallel to the direction of the fold axis. These foliations and lineations can themselves be deformed by later folding events. By identifying structural elements of successive folding events and mapping their spatial distributions and overprinting relationships, structural geologists are able to unravel complicated geological structures [e.g. O'dea et al., 2006; Armit et al., 2012].

In a typical field mapping campaign, a structural geologist will systematically record the orientation of foliation surfaces and associated lineations [Ramsay and Huber, 1987, p. 677-678]. These geometrical observations are typically interpreted and summarised onto a map as form lines. Fig. 1A shows the bedding trace of a small outcrop and Fig. 1B shows the relevant structural information that could be used to unravel the geometry of this outcrop from only selected areas. Form lines are usually a representation of the trend of observations and will often record at the scale of the map, the overprinting relationships that can be observed in and between outcrops [Alsop and Holdsworth, 1999; de Kemp, 2000; Lisle, 2003]. Form lines that represent the trace of the axial surface record the location of the fold hinge.

### 2.2 Implicit Fold Modeling

Laurent et al. [2016] use the structural elements of the fold (fold axis, axial foliation and fold vergence) to define additional orientation constraints for implicit modeling. A fold frame is defined with coordinates represented by 3D scalar fields, denoted as $x$, $y$ and $z$. Three local direction vectors ($e_x$, $e_y$ and $e_z$) are implicitly defined by the fold frame coordinates for any location and are used to define the relative orientation of deformed foliations and structural elements. One of the main ideas of the method is to use classical interpolation (and the associated isotropic smoothness assumption) on the least deformed surfaces defining the fold frame, then to use this information to allow for anisotropic interpolation of more deformed surfaces.

For example, to model the geometry of a structure resulting from two folding events, the axial surface ($S_2$) of the most recent fold ($F_2$) would be first modeled by interpolating field observations of the axial surface or associated foliation. The orientation of the axial surface ($S_1$) of the older folding event ($F_1$) can then be constrained with respect to ($S_2$) using a description of the fold geometry for $F_2$ folds. This additional orientation constraint is in turn used for interpolating $S_1$ geometry and the process is finally repeated for $S_0$. Locally the fold geometry is constrained using a global scalar field representing the angle between consecutive foliations, *e.g.* $S_1$ and $S_2$.

The local orientation of the folded surfaces can be characterised using the local direction vectors ($e_x$, $e_y$ and $e_z$) and two

rotation angles. The fold axis rotation angle rotates $e_y$ around $e_z$ to give the orientation of the fold axis ($L_i$). The orientation of the folded foliation ($S_{i-1}$) is characterised by rotating the whole fold frame around the fold axis $L_i$ by the fold limb rotation angle. The fold axis and fold limb rotation angles are the most important aspect of the fold modeling workflow because they control the geometry of the folded surface. The orientation of the folded surfaces need to fulfill the following criteria. It should be as close to the observations of the folded foliation as possible. Where no orientation constraints exist, the geometry of the folded foliation should fit the most geologically reasonable estimate, for example a folded surfaces should continue to be defined by localised variations in curvature away from observations instead of becoming a smooth surface [Jessell et al., 2014].

## 3 Fold Geostatistics

The fold axis ($\alpha_P$) and the fold limb ($\alpha_L$) rotation angles can be calculated for each observation of the folded foliation or lineation. Both $\alpha_P$ and $\alpha_L$ can range in value from $-90°$ to $90°$ (*e.g.* Fig. 2) and are $0°$ when the folded structural element is parallel to the direction of the fold frame coordinate. The larger the absolute value of a fold rotation angle, the larger the angle between the folded structural element and the fold frame. The geometry of the folded surfaces can be extracted by analysing the fold rotation angles within the fold frame coordinates.

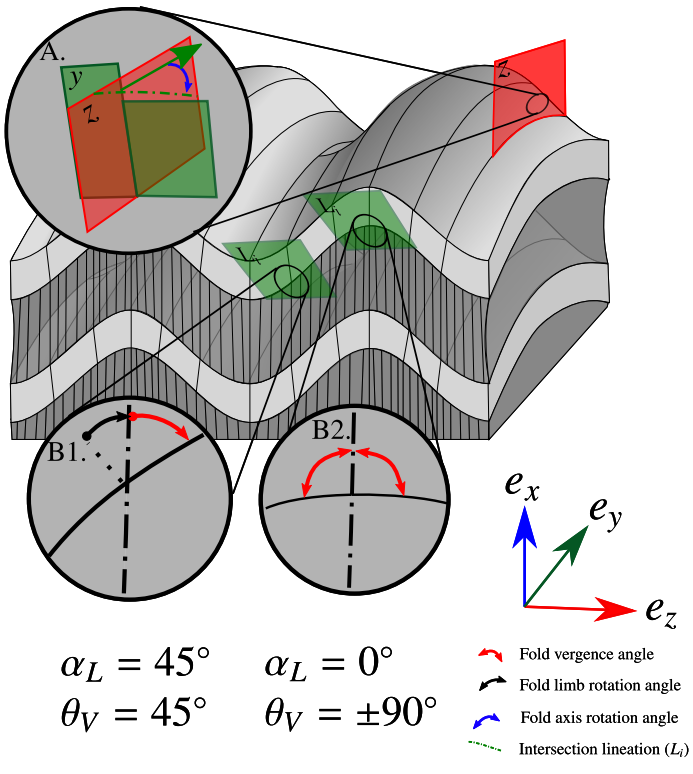


**Figure 2** Schematic fold sketch showing: A: Fold axis rotation angle is the angle between the lineation $L_i$ defining the local fold axis and $e_y$. B1: The fold limb rotation angle $\alpha_L$ is the angle between the normal to the folded foliation and the axial foliation, and is the complementary angle to fold vergence $\theta_v$. The fold limb rotation angle is $0°$ in the hinge of the fold (B2) and can reach $-90°$ or $90°$ in the limbs of a isoclinal fold.

### 3.1 Fold Axis Rotation Angle

The fold axis rotation angle ($\alpha_P$) is the angle between observations of the fold axis $L_i$ and $e_y$ (Fig. 2A) $\alpha_P$ is equivalent to the pitch of the fold axis in the axial surface of the fold if $e_y$ is horizontal. The fold axis is usually defined by field observations of the intersection lineation between the axial foliation and the folded foliation or by directly observing the hinge of a fold. To supplement these observations, which are often too sparse to characterise the geometry of the fold axis, we suggest to first interpolate the $z$ coordinate of the fold frame that represents the axial foliation ($S_{i-1}$) from available foliation observations. This interpolation makes sense as these these cleavage directions, which are more or less parallel to the fold axial surfaces, are generally smoother than the fold foliation ($S_i$). Even in the presence of cleavage refraction [Treagus, 1983], the intersection of this foliation field ($S_{i-1}$) with the folded foliation measurements ($S_i$) locally define the fold axis. A fold rotation axis angle of $0°$ means that the fold axis is parallel to $e_y$. For example, this would occur, in the peaks and troughs of a type 1 interference pattern. A cylindrical fold will have a constant $\alpha_P$ throughout the model, normally $0°$.

### 3.2 Fold Limb Rotation Angle

The fold limb rotation angle ($\alpha_L$) is the complementary angle to structural vergence. $\alpha_L$ is calculated by finding the complementary angle between $e_z$ and the normal to observations of the folded foliation ($S_{i-1}$) in the plane perpendicular to the fold axis ($L_i$) (Fig. 2B). For example an $\alpha_L$ value of $0°$ indicates the location of the fold hinge (Fig. 2B). The sign of $\alpha_L$ in the limbs of the fold is dependent on the $e_z$ direction.

### 3.3 S-Plot for analysing fold profiles

The S-Plot is a cross plot of either $\alpha_P$ or $\alpha_L$, and the associated fold frame coordinate. $\alpha_P$ is plotted against the $y$ coordinate, and $\alpha_L$ is plotted against the $z$ coordinate. The S-Plot allows for the characterisation of the effect of the younger deformation event on the geometry of the older structural feature independent of overprinting deformational events.

Fig. 3A shows a series of folded units with deformed axial surfaces. Fig. 3B is the fold shape viewed along the fold axis. Fig. 3C is the corresponding S-Plot to the 3D fold showing $\alpha_L$ plotted against the $z$ coordinate of the fold frame. In this case, the fold frame is folded, however the effects of that folding have no impact on the S-Plot for the older folding event. Because the S-Plot uses the fold frame coordinates, points are considered based on their location within the structure, *e.g.* the points i and ii in Fig. 3 are found on the same fold hinge (Fig. 3A) and occur at the same axial foliation scalar field value on the S-Plot (Fig. 3C). The S-Plot can be subdivided into three segments based on fold geometry: positive values of fold rotation angle characterise a fold limb (*e.g.* Fig. 3iii), negative values characterise an opposing fold limb (*e.g.* Fig. 3iv) and the location where the fold profile crosses 0 correspond to the fold hinge (*e.g.* Fig. 3i, ii).

The fold wavelength (distance in the $z$ coordinate of the fold frame for $\alpha_L$) can be identified by finding the location of two fold hinges and can be characterised for each fold closure independently. Synforms and antiforms can be differentiated by looking at the sign of the gradient of the fold profile for the hinge location. The sign of the rotation angle is dependent on the location chosen as the origin for the fold frame coordinates and on the polarity of the fold frame scalar field. When using scalar field interpolation

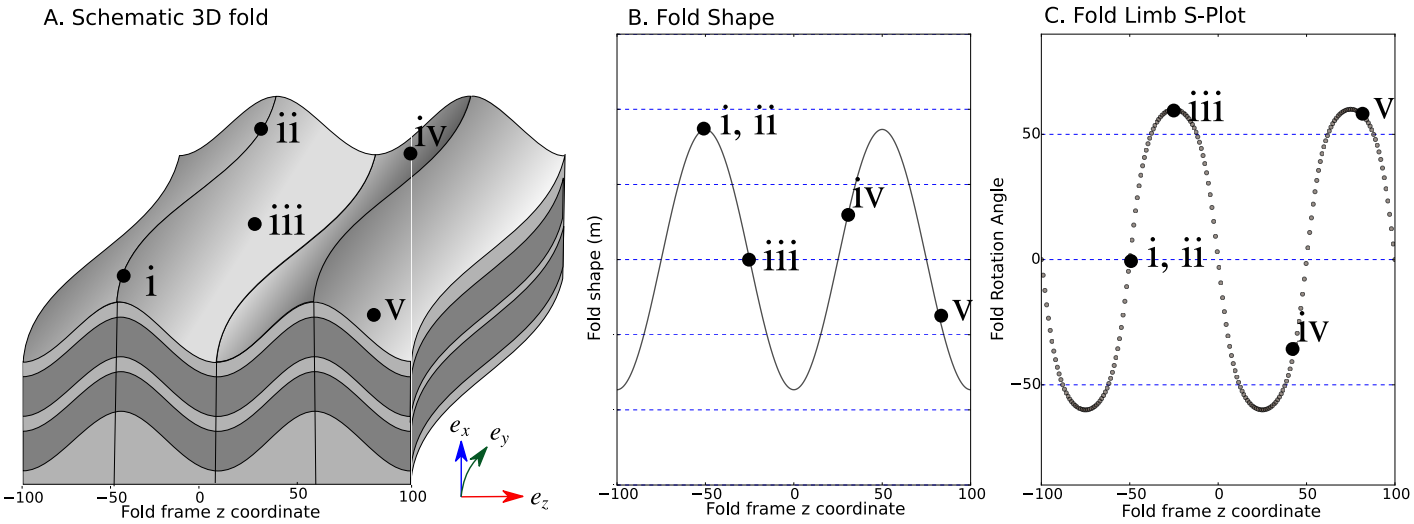


**Figure 3** A: 3D diagram showing folded surfaces with a deformed axial surface. *i* and *ii* are locations along the same fold hinge along the axial surface. *iii* corresponds to the point of inflection in one fold limb. *iv* and *v* are points on either limb of an antiform with a large Euclidean distance between them. B: Synthetic fold profiles representing the shape of the fold in the fold frame. The key locations in (A) are indicated in the fold profile. C: S-Plot showing fold rotation angle profile for the fold in (A) with the key locations indicated on the S-Plot. *i* and *iv* are closer in the fold frame coordinate than in Euclidean distance.

algorithms [Mallet, 2002; Cowan et al., 2003; Frank et al., 2007; Calcagno et al., 2008; Hillier et al., 2014] this can be controlled by specifying a normal constraint.

### 3.4 S-Variogram for analysing spatial correlation

Although folding results in rapid variations in the orientation of the folded surfaces, it also introduces structure into the spatial distribution of orientations. As a result of folding, two points that are close together will generally have similar orientations and pairs of points sampled in opposing limbs will systematically exhibit large variations. For periodical structures, points sampled at a distance close to any multiple of the fold wavelength will have a similar orientation. The spatial evolution of variability can be quantified using a sample semi-variogram [Chilès and Delfiner, 2008, p. 34], which plot the mean-squared-variance between pairs of points separated by a distance $h$. Such statistical tools are commonly used in geostatistics because they provide insight into spatial variability without requiring assumptions about the mean of the property being sampled [Chilès and Delfiner, 2008, p. 32].

Folded surfaces generally exhibit a strong anisotropy in the orientation of the surface relative to the structural elements of the fold (fold axis and axial surface). Changes of orientation are statistically smaller for pairs of points aligned along the axial foliation and higher for pairs of points aligned orthogonal to the axial foliation. Such anisotropy can be revealed by considering only pairs of points aligned in a specified direction.

Gumiaux et al. [2003] successfully apply this strategy for identifying trend in a fold series. The variogram value reaches local maximum values where the points are separated by half a wavelength present in the fold trend, and reaches a local minimum where the points are separated by a wavelength of the fold. A variogram calculated along the axial surface shows minimal changes in variance between the pairs.

The identification of a suitable coordinate system and direction of anisotropy is necessary for robustly characterising the fold wavelength. For example, a curvilinear distance defined by geological distances, *e.g.* down dip, along strike and across strike for measurements in folded beds [Chilès and Delfiner, 2008, p. 48]. The fold frame coordinate system [Laurent et al., 2016] provides a suitable coordinate system for characterising the geometry of the fold, even in the case of overprinting deformations. The S-Variogram is a sample semi-variogram calculated on the fold limb or axis rotation angle using the associated fold frame coordinate, respectively $y$ and $z$. The S-Variogram is defined as follows for a series of observations of fold rotation angles $\alpha_i$ at location $z_i$, with $i$ ranging from 1 to the number of observations:

$$\gamma(h) = \frac{1}{\left|\, 2N(h) \,\right|} \sum_{(i,j)\in(1,n)} \left|\, \alpha_i - \alpha_j \,\right|^2 \qquad (1)$$

The lag distance $h$, is the distance between two data points in a pair, *e.g.* $\left|\, z_i - z_j \,\right|$. $N(h)$ is the number of pairs in the set. In practice a lag distance tolerance is generally applied ($h \simeq |z_i - z_j|$) so that $N(h)$ is large enough to compute a reliable average. Each rotation angle is analysed using the associated fold frame coordinate. This means that the direction of anisotropy for the variogram is implicitly defined by the geometry of the fold frame.

The S-Variogram is used as an analytical tool to help characterise the fold geometries. If the experimental S-Variogram exhibits a periodical shape with a hole effect, the structural observations can be confidently interpreted as a fold train where the half wavelength between adjacent fold hinges is relatively regular Fig. 4A. In contrast, if the variogram does not show a periodic shape, there may be insufficient data for characterising the periodicity of the fold geometry or the fold may not have regular wavelengths between adjacent fold hinges (*e.g.* Fig. 4B). The S-Variogram provides a quantitative approach for analysing the fold geometry in terms of fold wavelength and periodicity, which are key fold characteristics. The location of the first local maximum on the S-Variogram will correspond to the shortest wavelength of the folding (where the folding has a regular wavelength). We propose using the gradient descent method [Cauchy, 1847] to identify this location by traversing the S-Variogram with increasing step sizes until the gradient to the nearest neighbour is negative. The gradient is estimated for each step distance by finding the best fit straight line to surrounding points. In most cases the data points will not be uniformly distributed throughout the fold frame, and the number of pairs for each lag distance may vary. If the local maxima for the variogram value is also a

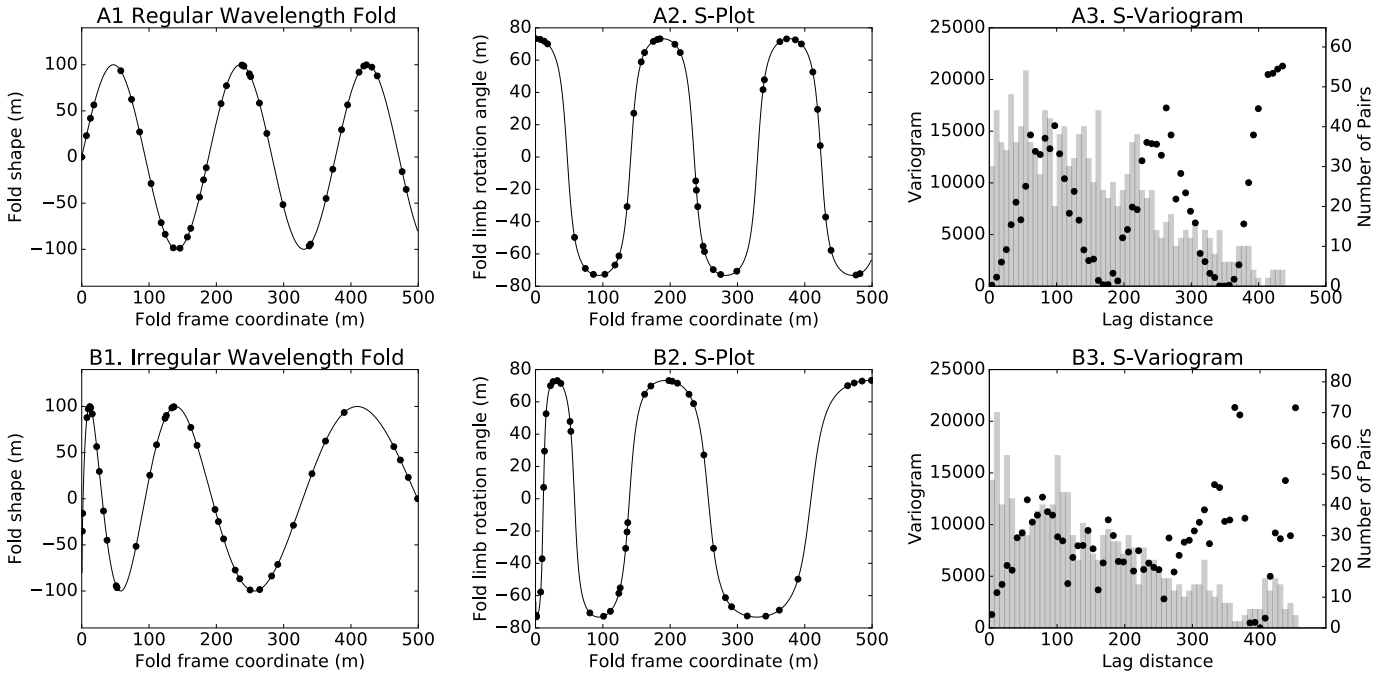


**Figure 4** A1: Fold geometry with regular wavelength between adjacent fold hinges, black dots showing 40 random sampling locations. A2: S-Plot for fold in (A1). A3: S-Variogram calculated on sample locations showing periodic results. B1: Fold geometry of irregular wavelength fold with black dots showing 40 random sample locatons . B2: S-Plot for fold in (B1). B3: S-Variogram for sample locations from (B1) with a subtle periodic trend.

local minima for the number of pairs, this estimate is not used. This methodology may also be used by varying the lag distance tolerance used to apply Eq. 1.

Choosing an appropriate step size for computing a sample variogram is not trivial and manual adjustments are often necessary in practice for obtaining good results. Here, we define a relatively robust strategy for making S-Variogram compatible with modeling without requiring too much user supervision. The proposed strategy is to chose a step size that is 20 percent larger than the average spacing between data points and a tolerance equal to the step size. This strategy yields reasonable results for the examples presented here and should apply to most structural data.

### 3.5 Synthetic Examples

In Fig. 5 three sinusoidal fold shapes of varying amplitude are shown. In these examples the wavelength of the fold have not been changed. As the amplitude of the fold increases, the tightness of the fold also increases. The folds range in tightness from blue (tightest), to red and green (most open). The tighter the fold, the steeper the gradient of the fold rotation angle where it crosses 0. This is consistent with structural geology observations where fold vergence will change quickly around the hinge when dealing with tighter folds. For isoclinal folds this will mean that identifying the locations of the fold hinges, or changes in fold vergence will be key to picking the appropriate fold geometry (which is usually the case in the field as well). This observation is also essential in the dip domains approach for modelling folds [Fernandez et al., 2009; Caumon et al., 2013].

Fig. 6 shows two different examples of asymmetrical folds that can be observed in the field. In Fig. 6A small scale folds occur within a larger scale antiform. The S-Plot showing the fold limb rotation angle for this example shows a series of small wavelength folds where the maximum and minimum rotation angles for the smaller scale fold decrease as the $z$ coordinate increases. The change in these extreme values with increasing $z$ coordinate represents the wavelength of the major antiform. The S-Variogram shows a periodic shape with the local maxima and minima representing the half wavelength and wavelength of the parasitic folds respectively. The S-Variogram can be used to robustly identify the half wavelength of the structure from irregularly spaced data for example in Fig. 4A.

A different type of asymmetrical fold can be observed in the field where the asymmetry is not associated with a larger scale folding event, or a folding event much larger than the study area. This could also be the result of the shortening direction of the fold not being orthogonal to the folded surface, for example when refolding a surface defined by a foliation. This type of asymmetrical fold and the associated S-Plot is shown in Fig. 6B. For each fold wavelength the features in the S-Plot for Fig. 6A and Fig. 6B are very similar. The maximum and minimum rotation angles remain constant for all folds in Fig. 6A.

## 4 Automatic Fold Modeling

The interpolation of the fold rotation angles is the most important stage of the structural modeling workflow proposed by Laurent et al. [2016] as the values of these rotation angles directly controls the orientation of the folded surfaces. The interpolation of angular data can be a complicated task and traditional statistical techniques are not necessarily applicable [Gumiaux et al., 2003]. For example, the fold rotation angles must be $< 90$ and $> -90$. We interpolate the fold rotation angle by representing the fold rotation angles as $\hat{\alpha} = \tan\ \alpha$. This results in the interpolated fold rotation angle values not exceeding the boundary conditions.

To capture the complex geometries that are seen in natural folds, the fold profile needs to be interpolated directly from the available structural data. The fold rotation angles can be interpolated within the fold frame coordinate using any standard one-

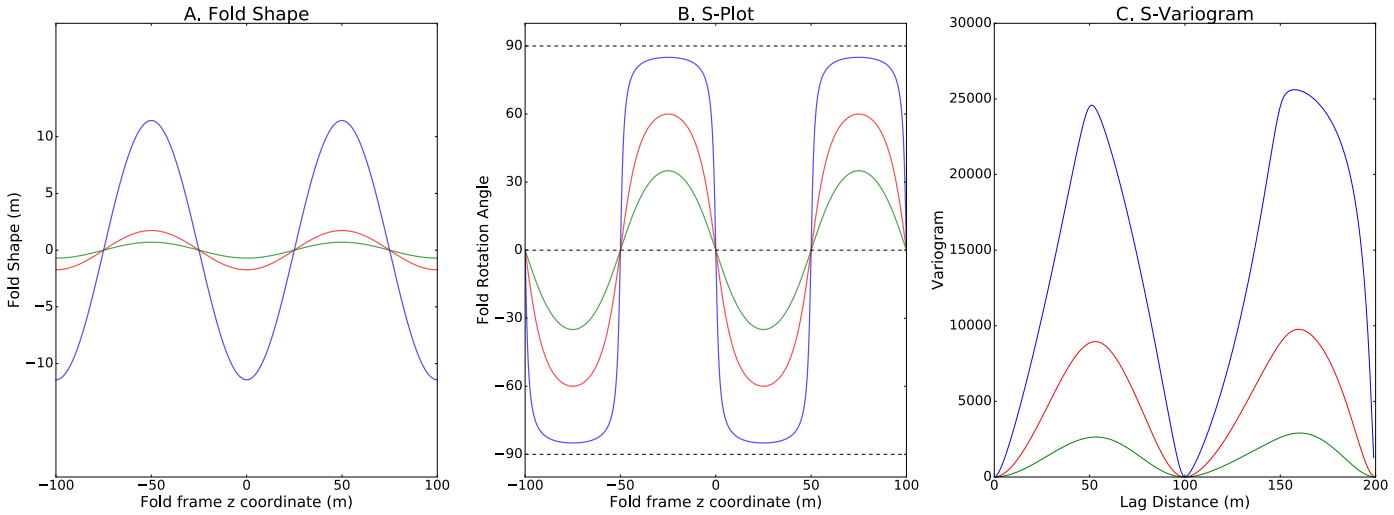


**Figure 5** A: Three fold geometry viewed looking along the fold axis. Blue line represents fold with largest amplitude, red and green have decreasing amplitudes. The fold shapes all have a wavelength of 100m. B. S-Plot for the fold profiles in (A) the colour of the S-Plot curve corresponds to the associated fold shape in (A). C: S-Variogram for the fold shapes in (A) and the colour of the S-Variogram curve corresponds to the associated curves in (A) and (B).

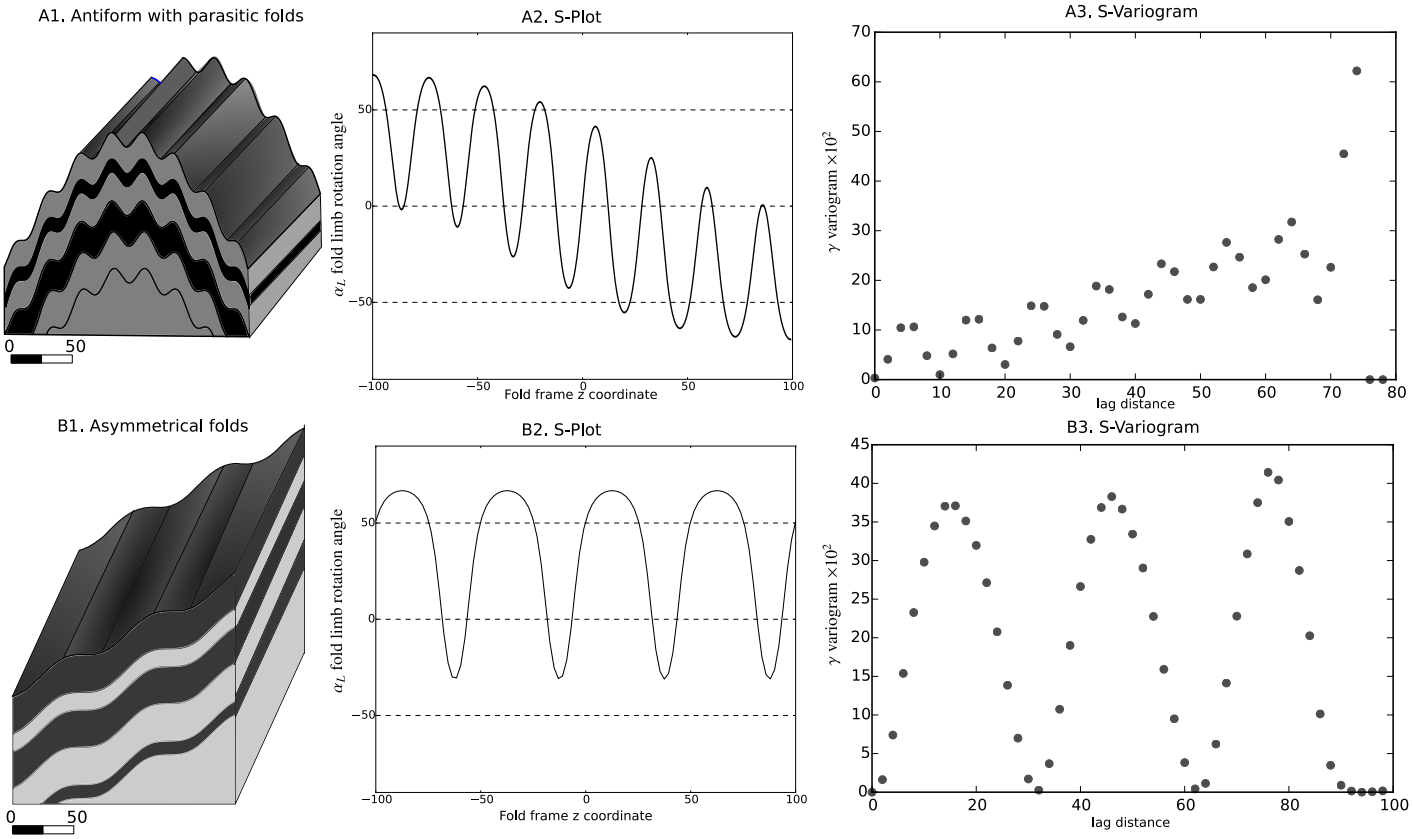


**Figure 6** A1: Large scale antiform with smaller parasitic folds. A2: S-Plot for fold limb rotation angle. A3: S-Variogram of fold limb rotation angle. B1: Asymmetrical folds. B2: S-Plot for fold limb rotation angle. B3: S-Variogram of fold limb rotation angle

dimensional interpolation algorithms (*e.g.* Splines, Kriging, Radial Basis Functions). This approach will work well when the geometry of the fold is regularly sampled in the S-Plot. Where the model area extends away from outcrops then these methods will most likely fail to capture the fold style. For example the fold series in Fig. 7A has samples from two outcrops capturing the geometry of two fold hinges separated by three unobserved fold hinges. The S-Plot in Fig. 7B shows the fold rotation angle for the observations (black dots) and the resulting interpolation using standard interpolation schemes. Three different basis functions, where the shape parameter is chosen to be the half wavelength of the fold (shown in Fig. 7C as the dashed line) are used for Radial Basis Function (RBF) interpolation. All three basis functions show similar results when interpolating within the half wavelength of the fold but generally deviate from the observed structural style when interpolating points further than a half wavelength from the nearest data point. This is because these methods tend to fit a smooth curve between structural observations and do not incorporate geological knowledge about the structural style of the folding [Jessell et al., 2014] (*e.g.* Fig. 7B).

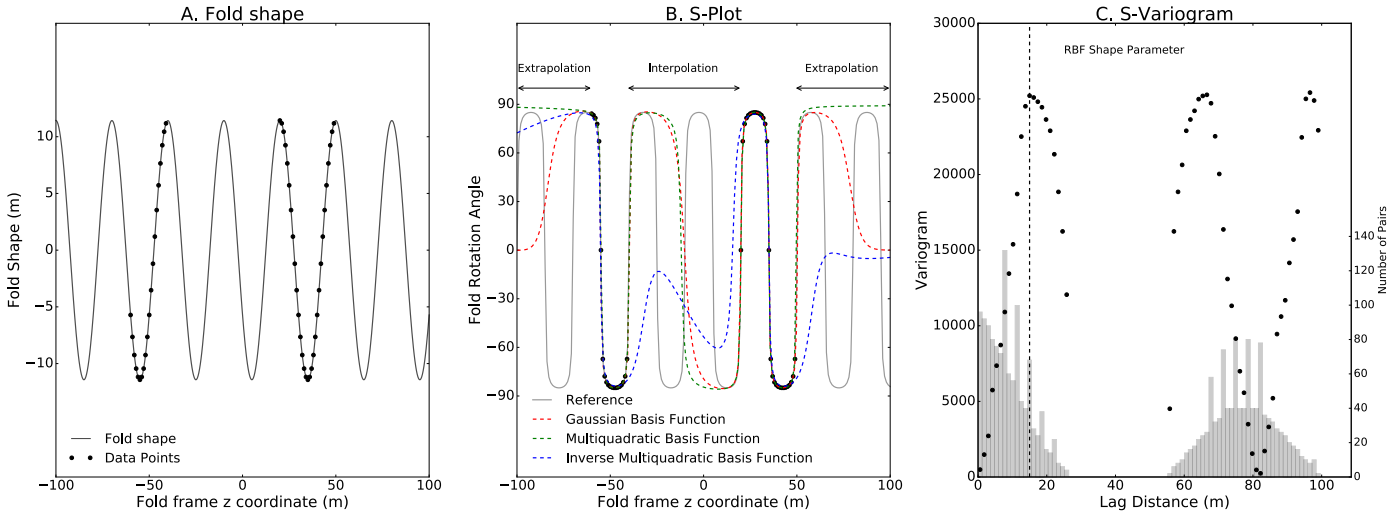


**Figure 7** A: Synthetic fold train sampled from two outcrop localities. B: Interpolation and extrapolation of the fold rotation angle using different basis functions with Radial Basis Function interpolation. C: S-Variogram of fold rotation angle, the vertical dashed line represents the shape parameter used for the basis functions.

To build a geologically reasonable estimation of the folding style the geologist will generally look at the surrounding structures, fold style and vergence to predict the location of fold closures. This is process is difficult to quantify and undertake objectively. The basic assumption that can be used to predict the geometry of folds between outcrops is a continuation of the same shape folding. For example, in Fig. 7 there are two outcrop locations sampled from a simple sinusoidal fold train. The geologically reasonable estimation for the fold geometry would be to continue the same shape between the outcrops. Using the S-Variogram, the periodicity of the folding can be tested and where this assumption is valid (where a hole effect is observed) the perodicity of the folding can be modeled by finding the best fit Fourier series to the available dataset. If the folding cannot be modeled using a periodic model and the data sufficiently describes the fold geometry this can be interpolated using standard interpolation. Here, we use a one- dimensional RBF interpolation scheme.

## 4.1 Interpolating fold geometries using Radial Basis Functions

Radial Basis Function (RBF) interpolation is a commonly used method for interpolating spatial data. RBF methods are used to approximate multivariate functions from data in n-dimensional space for observations of the function value [Buhmann and Levesley, 2004]. It is a widely accepted algorithm for interpolation in various scientific fields including applications to 3D geological modeling [Cowan et al., 2003; Hillier et al., 2014]. The RBF interpolant can be used in any dimensions as the interpolant is a function of distance between the points. We use the RBF interpolation algorithm to interpolate the 1D fold rotation angle profiles. The value of either fold rotation angle for the relevant fold coordinate ($z$ or $y$) is estimated using all observations of the fold rotation angle. A standard RBF interpolation approximates the unknown function, using the weighted sum of N radial basis functions ($\phi$) acting on the distance between the location being estimated $x$ and the location of the observations $x_i$.

$$\hat{\alpha}(x) = \sum_{i=1}^{N} \omega_i \, \phi(\|x - x_i\|) \tag{2}$$

A number of different basis functions, with different interpolation properties exists. Generally the basis functions have two parameters: a shape parameter $\sigma$ which is generally constant for all basis functions used in the interpolation and the distance between two points $r = \|x - x_i\|$. In this study we use a Gaussian basis function:

$$\phi(r) = e^{-(\frac{r}{\sigma})^2} \tag{3}$$

The shape parameter for the RBF adjusts the area of influence for particular data points. It controls the distance up to which a data point will significantly influence the interpolated value. It is comparable to the range of a semi-variogram model used for kriging interpolation. To interpolate the fold rotation angle we choose to use the range of the S-Variogram as the shape parameter for the RBF interpolation. The RBF interpolant is only used to interpolate the fold rotation angles where no interpolated locations are more than a half wavelength from the nearest data point. This criterion is used because folding is periodic and after a half wavelength of the fold the correlation between pairs of points separated by a half wavelength of the fold should increase (where the variogram value decreases). As the distance between points increases, the interpolant places less weight on the surrounding points, effectively reducing the correlation between observations, this would result in interpolation artefacts such as in Fig. 7B where the interpolant fails to capture the folding style.

## 4.2 Extrapolating fold geometries using Fourier series approximation

Early work on fold shape analysis used a Fourier series approximation of the fold shape [Stabler, 1968; Hudleston, 1973; Ramsay and Huber, 1987; Stowe, 1988]. The Fourier coefficients were optimized using least squares fitting of the coefficients for a known fold wavelength. This approach is suitable for analysing and representing the geometry of a single observable horizon looking along the fold axis. We propose using a Fourier series representation of the fold rotation angles to represent both the fold axis and fold limb rotation angles.

The Fourier series is a combination of trigonometric functions that can be used for approximating a periodic function. In its

standard form the Fourier series is:

$$\hat{\alpha}(x) = A_0 + \sum_{k=1}^{\infty} A_k \cos\frac{k\pi x}{\lambda} + B_k sin\frac{k\pi x}{\lambda} \quad (4)$$

where the Fourier coefficients $A_k, B_k$, represent the contribution of each frequency to the function being approximated. $\lambda$ represents the wavelength of the fundamental frequency of the periodic function being estimated. The wavelength of the fold can be automatically identified from the S-Variogram.

The values for a finite number of Fourier coefficients can be solved using least squares. To ensure that a solution can be found there needs to be a greater or equal number of data points to the number of coefficients being estimated. The coefficients $A_0, A_1, B_1, \ldots, A_k, B_k$ can then be used in the Fourier series (Eq. 4) to interpolate the fold rotation angle for any value of the fold frame scalar field.

The number of coefficients used controls the complexity of the fold geometry that is modelled. Irregular sampling, ambiguity and uncertainty in the structural observations can result in an overfitted Fourier series curve if too many coefficients are chosen. The interpolated fold rotation angle curve needs to be locally smooth while still describing the underlying fold shape. One way to control the resulting profile is to optimize the number of coefficients using a regularization approach with an objective function that assesses the required criteria. An alternative approach is to filter the noise from the data prior to fitting the Fourier series. To address irregular sampling which is problematic in Fourier analysis [Chilès and Delfiner, 2008, page 57], we propose using the RBF interpolation scheme prior to fitting the Fourier series where the interpolation is performed only on data points separated by less than the half wavelength of the fold.

## 5 Case studies

### 5.1 Proof of concept: Synthetic fold

Fig. 8A is a doubly plunging fold series generated in Noddy [Jessell and Valenta, 1996] using the python interface, pynoddy [Wellmann et al., 2016]. Two outcrops are used for sampling structural observations both located in fold hinges. The main folding (associated with $S_1$ axial foliation observations) in the reference model has a wavelength of 5000$m$ and an amplitude of 1000$m$. The doubly plunging effect is created by super imposing a second folding event with an axial surface perpendicular to the main folds axial surface creating a Type 1 fold interference pattern. Orientation measurements representing the orientation of the axial foliation ($S_1$) and the folded bedding surface ($S_0$) are shown on the geological map (Fig. 8B). The form lines shown on the geological map are not used to create the geological model and are only shown for highlighting the reference geometry. The axial surface of the fold train has a curvilinear geometry which can be seen by the subtle change in strike of $S_1$ in the northern outcrop. The $z$ coordinate of the fold frame is modelled using observations of $S_1$ (Fig. 9D). The interpolated $z$ coordinate captures the curvilinear geometry of the axial surface in the reference model. The $y$ coordinate is modelled using the constraints that $e_y$ is orthogonal to $e_z$ and is horizontal ensuring a unique solution for the scalar field (Fig. 9A). The intersection lineation is locally calculated by finding the intersection between $S_0$ and the isosurfaces of the interpolated $z$ coordinate scalar field. The fold axis rotation angle is calculated by finding the angle between the intersection lineation and $e_y$ in the plane perpendicular to $e_z$. The S-Variogram for the fold axis rotation angle can be seen in Fig. 9B. The number of pairs for each lag distance shows a significant drop between 1000$m$ and 2000$m$. This indicates there are not enough pairs of points in these locations to robustly estimate the variogram value. In order to avoid identifying the incorrect wavelength the number of pairs can be used to validate the identification of a local maxima. If the identified local maxima also corresponds with a local minima in the number of pairs (such as seen at a lag distance of 1000$m$ in Fig. 9B) this wavelength estimate is discarded. In this example the variogram value continues to increase at larger lag distances and neither a hole or sill effect can be observed. This suggest that the orientation data does not sample more than the fold half wavelength. In this case it is not possible to determine whether the folding has a regular wavelength distance or if the estimated wavelength is a true estimate of the fold wavelength.

We use the maximum lag distance of 3780$m$ for the S-Variogram as the RBF shape parameter. In this case the fold axis rotation angle only needs to be extrapolated a maximum of 1700$m$ away from the nearest data point. Fig. 9C shows the fold axis rotation angle calculated for the structural observations that are marked by black dots, the interpolated fold axis rotation angle profile inferred with a RBF interpolant (blue line) and using the Fourier series (black line). The interpolated profile is shown for the range of $y$ coordinate values in the model space (Fig. 9A). The two interpolation methods produce very similar results because minimal extrapolation is required. If the model area were extended further in the north (or south) then the difference between the two interpolation methods would be exaggerated. However, because the S-Variogram does not show a sill or hole effect, it is not possible to determine a good estimate for the fold wavelength. In these cases the wavelength may need to be refined by the geologist, or additional data must be collected to better constrain the geometry of the folding.

The fold axis is defined throughout the model space by locally rotating $e_y$ around $e_z$ using the interpolated fold axis rotation angle for the $y$ coordinate values. The fold limb rotation angle is calculated by finding the angle between the normal to the bedding orientation ($S_0$) and $e_y$ in the plane perpendicular to the interpolated fold axis. Fig. 9E shows the S-Variogram for the fold limb rotation angle in the $z$ coordinate, with a histogram representing the number of pairs of points for lag distance. The number of pairs is irregular with a low number of pairs occurring between 1500$m$ and 3500$m$. These lag distances are greater than the maximum distance within an outcrop and less than the distance between outcrops (Fig. 8B). There is a higher number of pairs at a lag distance greater than 4000$m$ correlating with a hole effect for the S-Variogram. A local maximum for the S-Variogram value is seen for a lag of 3000$m$, however this variogram value is also surrounded by lag distances with no data pairs. This suggests that the half wavelength of the fold is between 1500$m$ and 3000$m$ which is consistent with the reference model fold wavelength of 5000$m$. If the folding is symmetrical and has a regular wavelength between fold hinges a hole effect should be observed at a lag distance equal to the fold wavelength. In this case a hole effect is seen at 4000$m$ with a local mininimum occurring at 4500$m$. The hole effect seen at $\sim$ 4000$m$ is consistent for step distances between 200$m$ and 700$m$, the step distance in Fig. 9E is equal to the average nearest neighbour of $\sim$ 450$m$. Small variations in the estimated wavelength for different variogram step distances could be used to explore geological uncertainty associated with the fold geometry.

The S-Plot of the fold limb rotation angle (Fig. 9F) shows two populations of data points that correspond to the locations of the

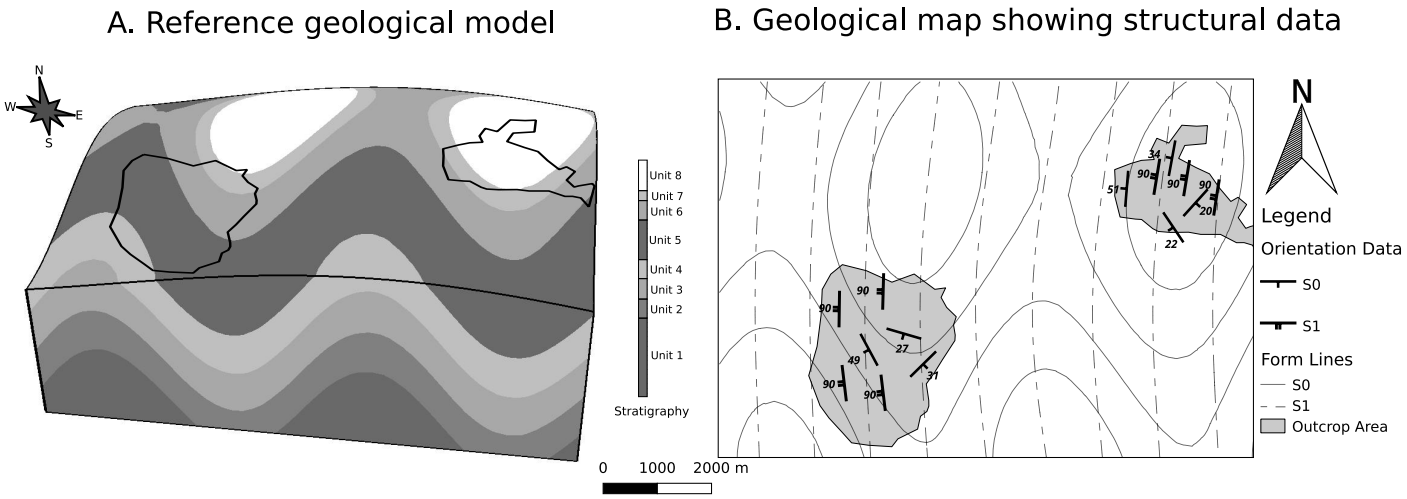


**Figure 8** A: Reference model of doubly plunging fold showing outcrop locations. B: Geological map showing outcrop locations with structural data and bedding form lines for model area.

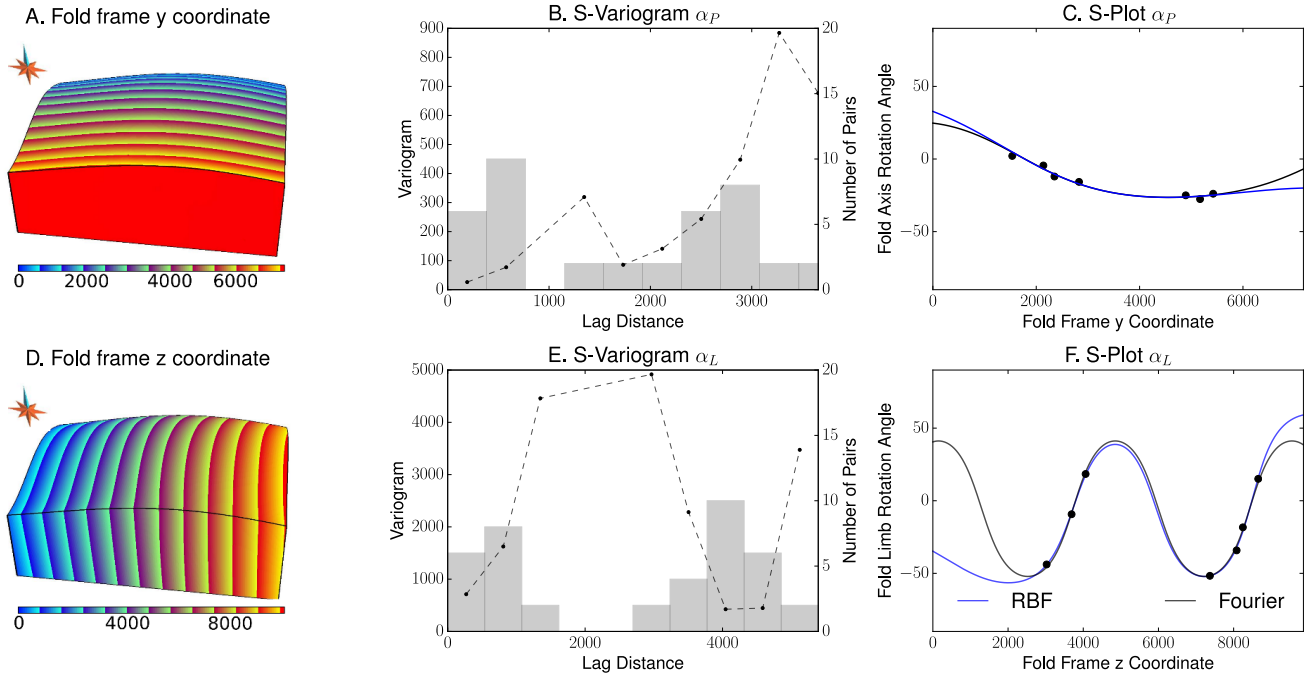


**Figure 9** A: Interpolated $y$ coordinate scalar field. B: S-Variogram of $\alpha_P$ with a step distance of 300$m$. C: S-Plot of $\alpha_P$ and $y$ showing the fold profile interpolated using an RBF interpolant (blue curve) and Fourier series (black curve). D: Interpolated $z$ coordinate scalar field. E: S-Variogram of $\alpha_L$ with a step distance of 500$m$. F: S-Plot of $\alpha_L$ and $z$ and interpolated fold profile using an RBF interpolant (blue curve) and Fourier series (black curve).

outcrops in Fig. 8B. To interpolate the fold rotation angle profile using the RBF interpolation scheme, we specify the shape parameter for the basis function as the half wavelength of the fold ($2250m$) and interpolate between the outcrop edges. The resulting interpolation using the RBF is shown in Fig. 9F using the blue curve and the Fourier series profile is shown by the black curve. The Fourier series is fitted to the RBF interpolated profile for the range of $z$ coordinate values for the data points (between 3000 and 8300). The main differences between the two interpolated profiles occurs where the fold geometry needs to be extrapolated. The Fourier series fold limb rotation angle curve continues the same structural style as observed in the outcrops. The RBF interpolation misses the fold hinge at $z = 1800m$, which roughly corresponds with the western fold hinge in the references model. In the eastern area of the model, less extrapolation is required and the differences between the interpolated fold rotation angle values is minimal and will not significantly impact the model geometries.

Each fold limb rotation angle profile will result in a different set of constraints for implicit modeling of the folded surfaces. The orientation of the folded surfaces are constrained by rotating the fold frame around the fold axis by the fold limb rotation angle. Using these constraints and the orientation observations of bedding from Fig. 8B, the model ($S_0$) is interpolated using Discrete Smooth Interpolation (DSI) [Mallet, 2002; Frank et al., 2007; Laurent et al., 2016]. The resulting model for both rotation angles being interpolated using the RBF scheme is shown in Fig. 10C. Fig. 10B is the resulting model interpolated using the Fourier series scheme for both rotation angles. The scalar field values of the interpolated models are constrained using a single data point in the north eastern outcrop. Both models deviate from the reference model in the western area due to the minimal value constraints used. This is intentional because the value constraints are integrated into the implicit scheme as equality constraints and if too many are used they can introduce significant geometrical artefacts. This problem could be solved using inequality constraints [Frank et al., 2007; Hillier et al., 2014] to constrain outcrop lithologies using a range of scalar field values rather than a single value or by the iterative process suggested by Collon et al. [2016].

Unit 5 is a good marker horizon for comparing the fold geometries. In the reference model (Fig. 10A) two antiforms can be seen and the north western area of the model shows a saddle structure. The Fourier series model Fig. 10B captures both antiforms, however the western antiform hinge location is shifted to the west. The saddle structure does not outcrop, however the geometry of the interpolated surfaces do capture this geometry. The difference in map pattern is most likely the result of the limited constraints used for the scalar field values because the dome structure is seen to the east of this antiform. The model interpolated with the RBF interpolant (Fig. 10C) only captures a single antiform. Along the axial surface the fold geometry of the two interpolated models and the reference model are very similar, all showing a non-cylindrical fold axis. The interpolated models have a fold axis that has been folded by a shorter wavelength fold ($7560m$) than the reference model ($13055m$). This is consistent with the S-Variogram analysis where it was not possible confidently estimate the fold wavelength. Both interpolated models capture the main fold geometry in the areas constrained by observations. The model interpolated from the using RBF interpolant does not capture the structural style away from observations and misses the continuation of the fold train. The Fourier series model captures the structural style of the reference model, however there are some variations in the outcropping geometry and location of fold hinges. These differences due to a combination of the sparse data and the location of samples relative to the fold geometry collected from the reference model.

### 5.2 Implicit Modeling of Cape Conran, Victoria

Finally, we present an application of the fold geostatistics and fold modeling [Laurent et al., 2016] to a case study from Cape Conran in the Palaeozoic Lachlan Fold belt, Eastern Victoria, Australia (Fig. 11A). The outcrop (location shown in Fig. 11B and a schematic structural map in C) is an asymmetric fold of a turbiditic sequence found in the limb of a larger antiform [Burg and Wilson, 1988]. There is a degree of disharmony in the fold geometries across different layers (mudstone and sandstone) of varying competency and thickness. We use field observations of the axial surfaces of folds (Fig. 11C, $S_1$) to interpolate the $z$ coordinate of the fold frame. The orientation of bedding ($S_0$), is representative of the folded sandstone layers and was collected in the field (Fig. 11C). The form lines shown in Fig. 11C show the interpreted structure from aerial imagery and the collected field observations. In this example, the form lines are not used in the modeling scheme and the geometrical model is based entirely on the orientation observations.

The scalar field representing the $z$ coordinate of the fold frame is interpolated using Discrete Smooth Interpolation (DSI) [Mallet, 2002; Frank et al., 2007] on the field observations ($S_1$ in Fig. 11C). To ensure a unique solution, the normals to the ($S_1$) foliation are all directed towards the east, imposing an eastward growing scalar field. The scalar field is shown in Fig. 12D and appears to conform well with the data and the geometry of the interpreted $S_1$ form lines. The fold axis is represented by the average direction of the intersection between observations of bedding and $e_z$, plunging 53° towards 356°. The fold limb rotation angle is calculated as the angle between field measurements of bedding $S_0$ and $e_z$ in the plane perpendicular to the fold axis. The S-Variogram of the fold limb rotation angle is shown in Fig. 12A. The lag distance for the variogram is equal to the average nearest neighbour distance and the number of pairs (indicated by the histogram) decreases with increasing step distance. The S-Variogram reaches a maximum value at approximately $0.57m$ and shows a hole effect at a lag distance of $0.7m$. The fold wavelength can be estimated to be $1.14m$. The discrepancy between the hole location and the wavelength estimate is most likely the result of the fold asymmetry and suggests that there is a difference between the length of the short limb wavelength and the long limb wavelengths. This is also the cause of the low variogram values from $0.7m$ to $1.3m$.

The geometry of the fold can be extracted using the S-Plot Fig. 12B and C. The negative values of the fold limb rotation angle correspond to the longer limbs of the fold and the positive the shorter limbs. The fold limb rotation angle data points show an asymmetrical shaped fold with a larger absolute value for maximum fold limb rotation angle for the longer limb. These characteristics are very similar to the pattern observed in the asymmetrical fold in Fig. 6B.

Fig. 12B shows the fold limb rotation angle interpolated using RBF interpolation with a shape parameter of $0.57m$. In the areas where the fold rotation angle is extrapolated away from the observations the, interpolation is biased towards the long limb of the fold (where the majority of observations occur). The resulting interpolated geometry captures the observed fold hinge well. However, away from the observations, there are no addi-

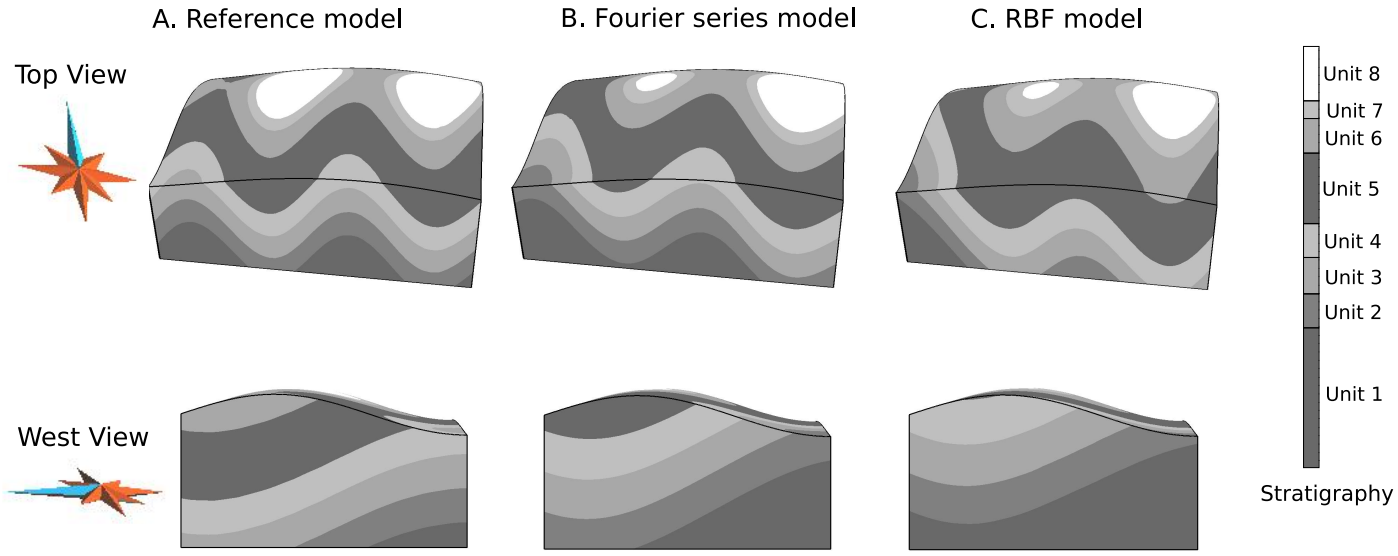


**Figure 10** A: Reference model looking from the top and from the west. B: Model interpolated using Fourier series for fold axis and limb rotation angles looking from the top and the west. C: Model interpolated using RBF series for fold axis and limb rotation angles looking from the top and the west.

tional folds and the model continues with the same geometry as the long limb of the fold. Given the input structural observations (Fig. 11B) where the folding is asymmetrical and there are no mapped structures that suggest the fold is not a part of a fold series, this model is probably not the most geologically reasonable approximation.

The Fourier series representation of the fold rotation angle (Fig. 12C) uses the estimated wavelength of the fold ($1.14m$) to create a regular periodical representation of the fold geometry. The Fourier series uses the fold geometry captured by the RBF interpolation of the data points within the outcrop to produce a continuation of the same structural style away from the outcrop. The resulting model fits the structural observations well and continues the same structural style away from the outcrop with an additional antiform to the east and a synform and antiform to the west.

In this example only a single short limb is captured by the structural observations making it difficult to determine from the data whether the asymmetrical fold is a parasitic fold associated with a larger wavelength fold (Fig. 6A) or whether the folding is asymmetrical folding unrelated to larger scale fold. In this case, regional context suggests that the asymmetrical folding is associated with a large antiform closing to the east of the model area [Burg and Wilson, 1988].

## 6 Discussion

Laurent et al. [2016] introduce a framework for modeling folds where the structural elements of folds (fold axes, axial foliation) and two rotation angles are used to define the orientation of the folded surface everywhere in the model. The use of this frame allows to simplify 3D fold analysis by considering variations along two one-dimensional profiles. This method is suitable to non-cylindrical structures, assuming the main shortening axis can be reliably obtained from the foliation associated to folding. In Laurent et al. [2016], the fold rotation angles are defined by estimating the geometry of the fold using a trial and error approach and fitting a modified sinusoidal fold geometry. In this contribution, we have addressed the main limitation in the method by using a data driven method for characterising and interpolating the fold rotation angles. We introduce two plots that allow for the geometry of the folds to be extracted from the available structural observations. The S-Plot shows the fold shape when looking down plunge of the fold and the fold axis rotation angle provides information about the non-cylindiricity of folding. The S-Variogram is used to test whether the fold wavelength is regular between observed fold hinges, and to estimate the dominant wavelength. These tools could be used during field mapping by the structural geologist to help understand the geometries of the structures being mapped and predict where more information is needed to characterise fold geometries.

The modified sinusoidal fold profile addresses two issues with classical implicit interpolation schemes highlighted by Jessell et al. [2014]: (1) the inability to interpolate or extrapolate fold series with continuous structural style; (2) the shape of fold hinges are not being controlled (and often being smoothed). In this contribution we directly interpolate the observed fold rotation angles to produce a model-wide representation of the fold rotation angles. The fold geostatistics are used to determine the appropriate interpolation method and the associated parameters for interpolation/extrapolation. The fold hinge geometry is characterised by the slope of the fold rotation angle curve at the hinge locations and is determined by the structural observations for each hinge where available or by extrapolating the geometry of the observed fold hinges. We believe this is advantageous because it is a data driven approach and the tightness of each observed fold hinge can be independently controlled by the structural observations.

In both Fig. 10 and Fig. 12, the fold geometries characterised using the Fourier series and the RBF interpolant are significantly different. The main differences between the resulting models are where extrapolation is required. In Fig. 12 the Fourier series model predicts a regular repetition of fold hinges away from the observations. The Fourier series model is based on the geometry of the observed single parasitic fold meaning the long limb distance between synform and antiform (measured in the z coordinate) is interpreted to be the same as the short limb distance. Without observing more fold hinges it is difficult to confidently constrain the appropriate wavelength value to use. However, the most geological reasonable estimation of the structure given the

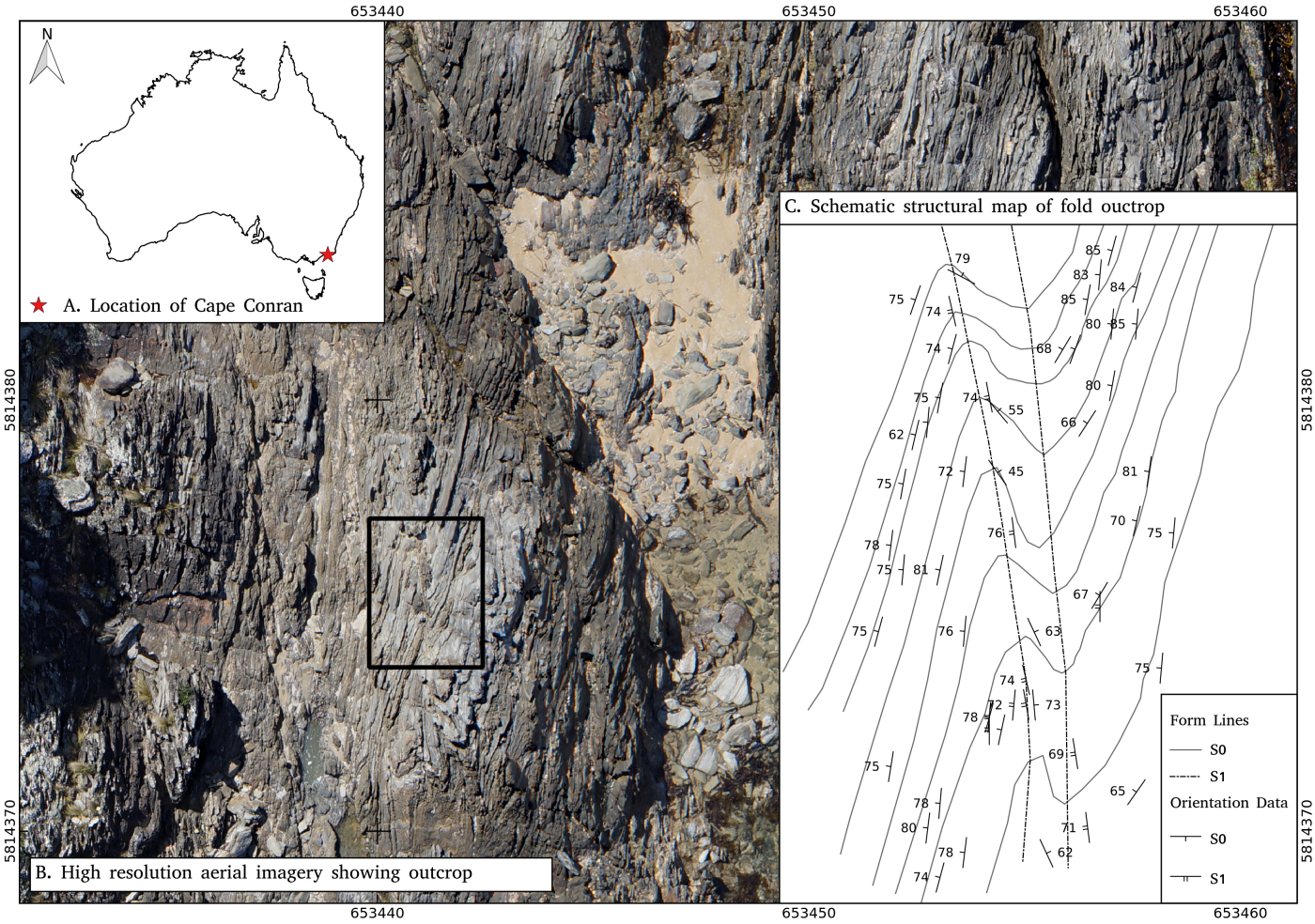


**Figure 11** A: Location of Cape Conran in the Palaeozoic Lachlan Fold belt, Eastern Victoria, Australia. B: Aerial photograph of rock platform depicting folded turbidite packages. C: Schematic structural map of outcrop used in this study.

available data is to continue the same structural style. If more data is collected, for example sampling another fold hinge at Cape Conran, the model can be updated using additional data.

The outcrop at Cape Conran has a high density of structural observations that capture the disharmony in the folding between the different sandstone layers. At the regional scale it is unlikey that enough structural observations and outcrops will be present to capture disharmony in folding. There are other sources for noise and uncertainty in the structural observations such as: geological uncertainty and ambiguity in observations and interpretations [Bond et al., 2007a,b; Jessell et al., 2010; Lindsay et al., 2012; Wellmann et al., 2010; Wellmann and Regenauer-Lieb, 2012]. Noise and irregular data sampling can add complexity to the model fitting process. Data points are evenly weighted and collocated data points can significantly skew the resulting model to a particular feature that may not be associated with the fold geometry. The use of the RBF interpolation prior to fitting the Fourier series model provides a suitable approach for filtering out the noise and uncertainty. The half wavelength of the fold is used to constrain the shape parameter for the basis functions. This will remove noise and ambiguity from the observed data for the model fitting without smoothing out the information associated with the folding.

The linear regression used to find the best fit Fourier series requires the largest fold wavelength to be known. This is identified by finding the range of the S-Variogram using the gradient descent method. The Fourier coefficients are optimised to find the best fit Fourier series for the given base wavelength. If the wavelength is underestimated, then the largest wavelength of the fold cannot be modeled. In contrast, if the wavelength is too large the extrapolated fold geometries may not be geologically reasonable. While the method is generally adequate for finding the best fit Fourier series, it may fail in the cases, where there is additional noise or where the half wavelength of the fold is not visible in the S-Variogram. In these cases, the wavelength could be specified by the geologist and refined to fit the observations. As shown in Fig. 9E the S-Variogram is limited by the spatial distribution of the structural observations. If there are not enough observations separated by the fold half wavelength, it is not possible to confidently estimate the half wavelength of the fold. Another limitation in this method is the resolution of the wavelength estimate will be dependent on the step distance of the S-Variogram. It would be beneficial to optimise the wavelength parameter as well as the Fourier coefficients, using a non-linear least squares approach.

A single best fit model was produced for the observed structural data. In Fig. 12 the range in the fold rotation angles for the long limb of the fold is ±15°. A single fold rotation angle curve cannot represent the range in possible fold geometries that could be fitted to these observations. Preliminary work using Bayesian inference to solve the Fourier series regression has provided promising results providing a range in possible fold geometries that could be fitted to the structural observations.

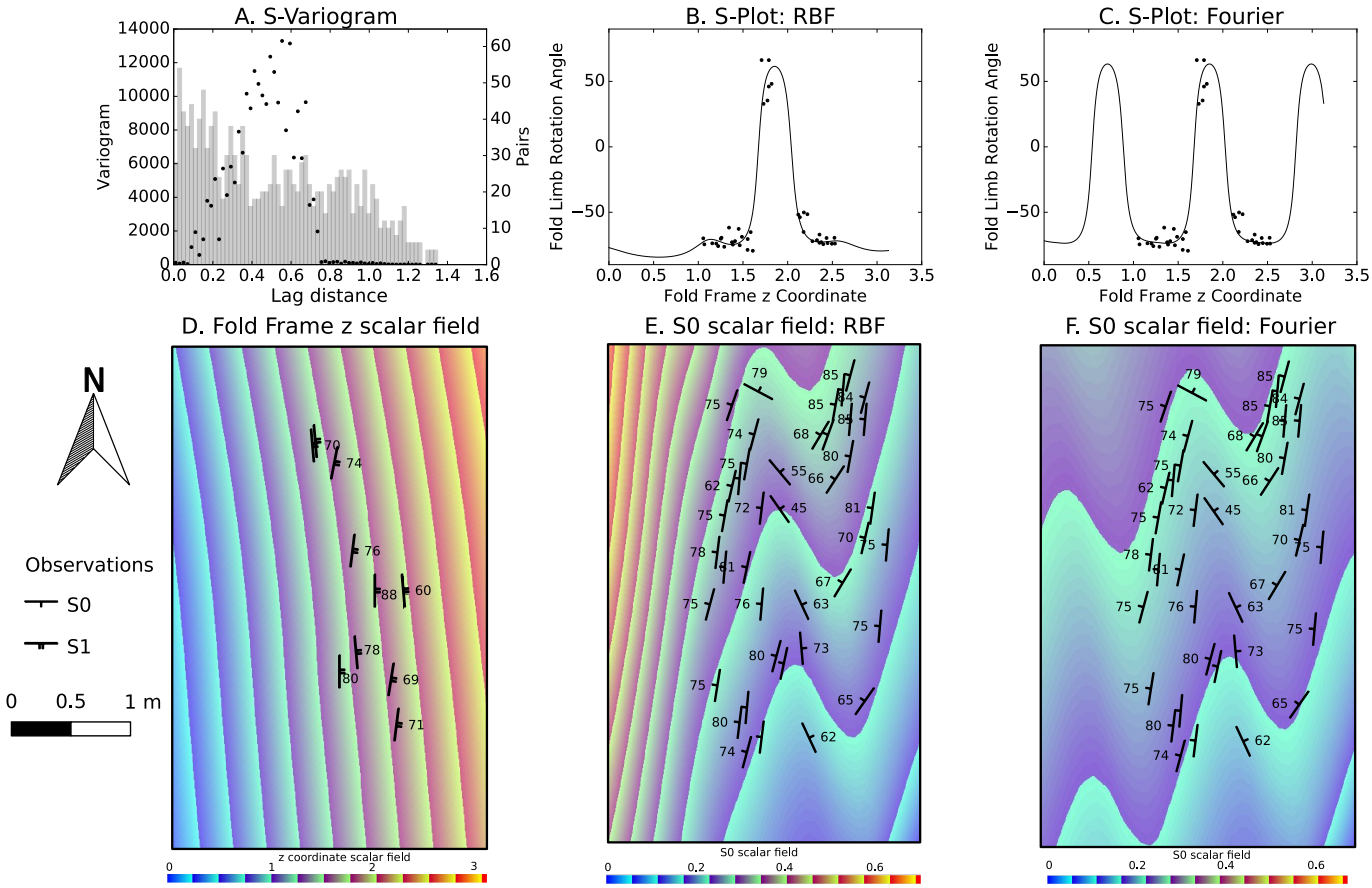


**Figure 12** A: S-Variogram of fold limb rotation angle. B: S-Plot with RBF interpolated fold rotation angle curve. C: S-Plot with Fourier series fold rotation angle curve. D: Scalar field representing the fold frame $z$ coordinate viewed from above. E: Scalar field representing bedding using the fold geometry constrained using the RBF curve viewed from above. F: Scalar field representing bedding using the fold geometry constrained by the Fourier series curve viewed from above.

## 7 Conclusion

In this contribution we have expanded the capabilities of the fold modeling framework presented in Laurent et al. [2016] by using structural data to directly inform the modeled fold geometry. Two main contributions to geological modeling and structural geology are presented in this paper:

- The fold geostatistic (S-Plot and S-Variogram) allow for the geometry of folds to be characterised directly from the field structural observations.
- The representation of the fold geometry using a Fourier series fitted to the structural observations produces a geologically reasonable extrapolation of the fold shape.

We have demonstrated an application of these tools to fold modeling with a proof of concept synthetic model and a more complicated asymmetrical fold from the Cape Conran, Victoria. We have primarily focused on the application of the fold geostatistics for geometrical modeling, however we also expect that these tools can be applied for structural analysis of folds. The representation of the fold geometry using a Fourier series has provided more flexibility in the possible fold geometry, allowing for a complex asymmetrical fold to be modeled, which was not possible to model using the previous methodology. Further developments are required to incorporate structural uncertainties into this work flow.

## Acknowledgements

The authors would like to thank Peter Hudleston and an anonymous reviewer for their comments that significantly improved this manuscript. This research was partially funded by Australian Research Council Discovery grant DP110102531 and Australian Research Council Linkage grant LP140100267. Part of this work was performed in the framework of the "Investissements d'avenir" Labex RESSOURCES21 (ANR-10-LABX-21) and of the RING project at Université de Lorraine. The authors are grateful to the industrial and academic sponsors of the Gocad Research Consortium managed by ASGA (Association Scientifique pour la Géologie et ses Applications, http://ring.georessources.univ-lorraine.fr/) for their support. We thank Paradigm for providing the GOCAD-SKUA software and API. All of the models in this publication have been generated with the StructuralFactory plugin for Gocad, based on RING's StructuralLab plugin. The synthetic dataset in Fig. 8 was generated using Noddy.

## References

G. I. Alsop and R. E. Holdsworth. Vergence and facing patterns in large-scale sheath folds. *Journal of Structural Geology*, 21(10):1335–1349, 1999. ISSN 01918141. doi: 10.1016/S0191-8141(99)00099-1. *(Cited page 2)*

R. J. Armit, P. G. Betts, B. F. Schaefer, and L. Ailleres. Constraints on long-lived Mesoproterozoic and Palaeozoic deformational events and crustal architecture in the northern Mount Painter Province, Australia. *Gondwana Research*, 22 (1):207–226, jul 2012. ISSN 1342937X. doi: 10.1016/j.gr.2011.11.003. *(Cited page 2)*

C. Aug, J.-P. Chilès, G. Courrioux, and C. Lajaunie. 3D Geological Modelling and Uncertainty: The Potential-field Method. In O. Leuangthong and C. Deutsch, editors, *Geostatistics Banff 2004*, volume 31, pages 145–154. Springer Netherlands, 2005. ISBN 978-1-4020-3515-9. doi: 10.1007/978-1-4020-3610-1{_}15. *(Cited page 1)*

C. E. Bond, A. D. Gibbs, Z. K. Shipton, and S. Jones. What do you think this is? Conceptual uncertainty in geoscience interpretation. *GSA Today*, 17:4, 2007a. ISSN 1052-5173. *(Cited page 12)*

C. E. Bond, Z. K. Shipton, R. R. Jones, R. W. H. Butler, and A. D. Gibbs. Knowledge transfer in a digital world: Field data acquisition, uncertainty, Visualization, and data management. *Geosphere*, 3:568–576, 2007b. ISSN 1553-040 (ISSN). *(Cited page 12)*

M. D. Buhmann and J. Levesley. Radial Basis Functions: Theory and Implementations. *Mathematics of Computation*, 73(247):1578–1581, 2004. ISSN 1941-6016. doi: 10.1017/CBO9780511543241. *(Cited page 7)*

J. J. Burg and C. J. L. C. Wilson. A kinematic analysis of the southernmost part of the Bega Batholith. *Australian Journal of Earth Sciences*, 35:1–13, 1988. ISSN 0812-0099. doi: 10.1080/08120098808729435. *(Cited pages 10 and 11)*

P. Calcagno, J. P. Chilès, G. Courrioux, and A. Guillen. Geological modelling from field data and geological knowledge. *Physics of the Earth and Planetary Interiors*, 171(1-4):147–157, dec 2008. ISSN 00319201. *(Cited pages 1 and 4)*

A. Cauchy. Méthode générale pour la résolution des systemes d'équations simultanées. *Comp. Rend. Sci. Paris*, (2):2–4, 1847. *(Cited page 4)*

G. Caumon, C. H. Sword Jr., and J.-L. Mallet. Constrained modifications of non-manifold B-reps. In *Proceedings of the Symposium on Solid Modeling and Applications*, pages 310–315, 2003. *(Cited page 1)*

G. Caumon, G. Gray, C. Antoine, and M.-O. Titeux. Three-Dimensional Implicit Stratigraphic Model Building From Remote Sensing Data on Tetrahedral Meshes: Theory and Application to a Regional Model of La Popa Basin, NE Mexico. *IEEE Transactions on Geoscience and Remote Sensing*, 51(3): 1613–1621, mar 2013. ISSN 0196-2892. doi: 10.1109/TGRS.2012.2207727. *(Cited pages 1 and 5)*

J.-P. Chilès and P. Delfiner. Conditional Simulations. *Geostatistics*, pages 449–592, 2008. doi: 10.1002/9780470316993.ch7. *(Cited pages 4 and 8)*

P. Collon, A. Pichat, C. Kergaravat, A. Botella, G. Caumon, J.-C. Ringenbach, and J.-P. Callot. 3D modeling from outcrop data in a salt tectonic context: Example from the Inceyol minibasin, Sivas Basin, Turkey. *Interpretation*, 4 (3):SM17–SM31, 2016. ISSN 2324-8858. doi: 10.1190/INT-2015-0178.1. *(Cited page 10)*

E. Cowan, R. Beatson, H. Ross, W. Fright, T. McLennan, T. Evans, J. Carr, R. Lane, D. Bright, A. Gillman, P. Oshust, and M. Titley. Practical implicit geological modelling. *5th International Mining Geology Conference*, (8): 89–99, 2003. ISSN 01489062. *(Cited pages 1, 4, and 7)*

E. a. de Kemp. 3-D visualization of structural field data: examples from the Archean Caopatina Formation, Abitibi greenstone belt, Québec, Canada. *Computers & Geosciences*, 26:509–530, 2000. ISSN 00983004. doi: 10.1016/S0098-3004(99)00142-9. *(Cited page 2)*

O. Fernandez, S. Jones, N. Armstrong, G. Johnson, A. Ravaglia, and J. A. Munoz. Automated tools within workflows for 3D structural construction from surface and subsurface data. *GeoInformatica*, 13(3):291–304, 2009. ISSN 13846175. doi: 10.1007/s10707-008-0059-y. *(Cited page 5)*

T. Frank, A.-L. Tertois, and J.-L. Mallet. 3D-reconstruction of complex geological interfaces from irregularly distributed and noisy point data. *Computers & Geosciences*, 33(7):932–943, jul 2007. ISSN 00983004. doi: 10.1016/j.cageo.2006.11.014. *(Cited pages 1, 4, and 10)*

C. Gumiaux, D. Gapais, and J. P. Brun. Geostatistics applied to best-fit interpolation of orientation data. *Tectonophysics*, 376(3-4):241–259, 2003. ISSN 00401951. doi: 10.1016/j.tecto.2003.08.008. *(Cited pages 4 and 5)*

C. Hilgers. Christoph Hilgers Scotland Schottland field trip page, 2006. *(Cited page 2)*

M. J. Hillier, E. M. Schetselaar, E. a. de Kemp, and G. Perron. Three-Dimensional Modelling of Geological Surfaces Using Generalized Interpolation with Radial Basis Functions. *Mathematical Geosciences*, pages 931–953, jul 2014. ISSN 1874-8961. doi: 10.1007/s11004-014-9540-3. *(Cited pages 1, 4, 7, and 10)*

P. Hudleston. Fold morphology and some geometrical implications of theories of fold development. *Tectonophysics*, 16(1-2):1–46, 1973. ISSN 00401951. doi: 10.1016/0040-1951(73)90129-7. *(Cited page 7)*

P. J. Hudleston and S. H. Treagus. Information from folds: A review. *Journal of Structural Geology*, 32(12):2042–2071, dec 2010. ISSN 01918141. doi: 10.1016/j.jsg.2010.08.011. *(Cited page 2)*

M. Jessell, L. Aillères, E. D. Kemp, M. Lindsay, F. Wellmann, M. Hillier, G. Laurent, T. Carmichael, and R. Martin. Next generation 3D geological modelling and inversion. 2014. *(Cited pages 1, 3, 6, and 11)*

M. W. Jessell and R. K. Valenta. Structural geophysics: integrated structural and geophysical modelling. *Computer Methods in the Geosciences*, 15:303–324, 1996. *(Cited page 8)*

M. W. Jessell, L. Ailleres, and E. a. de Kemp. Towards an integrated inversion of geoscientific data: What price of geology? *Tectonophysics*, 490 (3-4):294–306, jul 2010. ISSN 00401951. doi: 10.1016/j.tecto.2010.05.020. *(Cited pages 1 and 12)*

G. Laurent, L. Ailleres, L. Grose, G. Caumon, M. Jessell, and R. Armit. Implicit modeling of folds and overprinting deformation. *Earth and Planetary Science Letters*, 456:26–38, 2016. ISSN 0012821X. doi: 10.1016/j.epsl.2016.09.040. *(Cited pages 1, 2, 4, 5, 10, 11, and 13)*

M. D. Lindsay, L. Aillères, M. W. Jessell, E. a. de Kemp, and P. G. Betts. Locating and quantifying geological uncertainty in three-dimensional models: Analysis of the Gippsland Basin, southeastern Australia. *Tectonophysics*, 546-547:10–27, 2012. ISSN 00401951. doi: 10.1016/j.tecto.2012.04.007. *(Cited page 12)*

R. J. Lisle. Geological Structures and Maps. *Geological Structures and Maps*, pages 1–106, 2003. doi: http://dx.doi.org/10.1016/B978-075065780-8/50002-1. *(Cited page 2)*

R. J. Lisle and N. C. Toimil. Defining folds on three-dimensional surfaces. *Geology*, 35(6):519–522, 2007. ISSN 00917613. doi: 10.1130/G23207A.1. *(Cited page 1)*

J.-l. Mallet. *Geomodeling*. Oxford University Press, New York, NY, USA, 2002. *(Cited pages 4 and 10)*

C. Massiot and G. Caumon. Accounting for axial directions, cleavages and folding style during 3D structural modeling. In *30th Gocad Meeting Proceedings*, 2010. *(Cited page 1)*

M. Maxelon, P. Renard, G. Courrioux, M. Braendli, and N. S. Mancktelow. A workflow to facilitate three-dimensional geometrical modelling of complex poly-deformed geological units. *Computers & Geosciences*, 35:644–658, 2009. ISSN 0098-3004. *(Cited page 1)*

R. Moyen, J.-L. Mallet, T. Frank, B. Leflon, and J.-J. Royer. 3D-Parameterization of the 3D geological space - The GeoChron model. *Proc. European Conference on the Mathematics of Oil Recovery (ECMOR IX)*, (September):8, 2004. *(Cited page 1)*

I. Mynatt, S. Bergbauer, and D. D. Pollard. Using differential geometry to describe 3-D folds. *Journal of Structural Geology*, 29(7):1256–1266, 2007. ISSN 01918141. doi: 10.1016/j.jsg.2007.02.006. *(Cited page 1)*

M. G. O'dea, P. G. Betts, T. MacCready, and L. Aillères. Sequential development of a mid-crustal fold-thrust complex: evidence from the Mitakoodi Culminationin the eastern Mt Isa Inlier, Australia. *Australian Journal of Earth Sciences*, 53(March 2015):69–90, 2006. ISSN 0812-0099. doi: 10.1080/08120090500432447. *(Cited page 2)*

J. G. Ramsay and M. I. Huber. *The techniques of modern structural geology, Volume 2: Folds and fractures*. Academic Press, 1987. *(Cited pages 1, 2, and 7)*

C. L. Stabler. Simplified Fourier analysis of fold shapes. *Tectonophysics*, 6 (4):343–350, 1968. ISSN 00401951. doi: 10.1016/0040-1951(68)90049-8. *(Cited page 7)*

C. W. Stowe. Application of Fourier analysis for computer representation of fold profiles. *Tectonophysics*, 156(3-4):303–311, 1988. ISSN 00401951. doi: 10.1016/0040-1951(88)90067-4. *(Cited page 7)*

B. Thibert, J. P. Gratier, and J. M. Morvan. A direct method for modeling and unfolding developable surfaces and its application to the Ventura Basin (California). *Journal of Structural Geology*, 27(2):303–316, 2005. ISSN 01918141. doi: 10.1016/j.jsg.2004.08.011. *(Cited page 1)*

S. H. Treagus. A theory of finite strain variation through contrasting layers, and its bearing on cleavage refraction. *Journal of Structural Geology*, 5(3-4):351–368, 1983. ISSN 01918141. doi: 10.1016/0191-8141(83)90023-8. *(Cited page 3)*

J. F. Wellmann and K. Regenauer-Lieb. Uncertainties have a meaning: Information entropy as a quality measure for 3-D geological models. *Tectonophysics*, 526-529:207–216, 2012. ISSN 00401951. doi: 10.1016/j.tecto.2011.05.001. *(Cited page 12)*

J. F. Wellmann, F. G. Horowitz, E. Schill, and K. Regenauer-Lieb. Towards incorporating uncertainty of structural data in 3D geological inversion. *Tectonophysics*, 490(3-4):141–151, 2010. ISSN 00401951. doi: 10.1016/j.tecto.2010.04.022. *(Cited page 12)*

J. F. Wellmann, S. T. Thiele, M. D. Lindsay, M. W. Jessell, and J. Abc. pynoddy 1 . 0 : an experimental platform for automated 3-D kinematic and potential field modelling. pages 1019–1035, 2016. doi: 10.5194/gmd-9-1019-2016. *(Cited page 8)*